PAPER

Check for updates

A high lipid-soluble probe for ONOO⁻ recognition in the endoplasmic reticulum and imaging of cerebral ischemia-reperfusion injury

Yu-An Feng,† Zi-Hao Liu,† Wei Du, Ya-Wen Wang (ID) * and Yu Peng*

Cerebral ischemia/reperfusion injury (CIRI) is a highly damaging pathological process in stroke. In CIRI, ER stress is the main source of cellular reactive oxygen species (ROS) and significantly contributes to neurological damage. Among ROS, peroxynitrite (ONOO⁻) exhibits potent oxidative and nucleophilic properties. Monitoring ONOO⁻ within the ER is essential for understanding and treating CIRI. However, the lack of probes capable of crossing the blood–brain barrier (BBB) and selectively targeting the ER has hindered progress in this field. To address this challenge, we developed a near-infrared fluorescent probe, **SWJT-27**, which was designed for both BBB penetration and ER-specific localization. This probe demonstrated high reactivity and superior lipid solubility. The *in vitro* BBB model assays confirmed its efficient BBB permeability, while imaging studies revealed its ability to dynamically monitor ER-associated ONOO⁻ under various conditions.

Introduction

Cerebral ischemia-reperfusion injury (CIRI) is the most detrimental pathological process in stroke, driven by multifactorial factors including oxidative stress and inflammatory responses.[1,2] Although ischemia alone does not induce extensive tissue damage, the restoration of blood flow can trigger a surge in reactive oxygen species (ROS). These ROS react with cellular components, leading to structural damage and metabolic dysfunction.[3–5] Endoplasmic reticulum (ER) stress plays a pivotal role in cerebral ischemic injury. The occurrence of cerebral ischemia disrupts ER function, leading to ATP depletion, calcium dyshomeostasis, and oxidative stress. Notably, ROS generated during oxidative stress directly damage ER proteins and lipids, resulting in protein misfolding and functional impairment.[6,7] Consequently, detecting and visualizing ER-specific ROS during CIRI is crucial for developing targeted therapeutic strategies.

Peroxynitrite (ONOO⁻), a common ROS synthesized from NO and superoxide anions, is abundantly generated during the CIRI process.[8] It exhibits strong oxidative and nucleophilic properties, enabling it to react with cellular proteins and nucleic acids, ultimately triggering the apoptotic pathway.[9–11]

Due to its crucial role in oxidative stress, ONOO⁻ detection can serve as a valuable indicator for assessing oxidative damage. However, the accurate measurement of ONOO⁻ remains challenging owing to its short half-life and rapid decomposition kinetics, which requires the development of highly sensitive detection methods.[12,13]

In recent years, fluorescence imaging has emerged as the primary method for ONOO⁻ detection, replacing many traditional methods (including magnetic resonance imaging, electrochemical methods and electron spin resonance).[14–22] It has the advantages of high sensitivity, good biocompatibility and strong modifiability and has been successfully used for monitoring ONOO⁻ in various pathological conditions, including tumors,[23] hepatic ischemia,[24] and acute lung injury.[25] Despite these advances, the application of fluorescent probes for ONOO⁻ detection in CIRI is still limited, primarily due to the hindrance of the BBB. Its selective permeability can prevent hydrophilic substances, charged molecules, proteins and the vast majority of fluorescent probes from entering the brain.[26,27] Brain microvascular endothelial cells (BMECs) are a critical component of the BBB, selectively restricting molecular penetration and permitting only small and lipophilic molecules to pass through. While passive diffusion enables small molecules to traverse the BBB, this process depends on specific properties, including low molecular weight, minimal polar surface area, limited hydrogen bond donors, and high lipophilicity.[28–30] There are almost no fluorescent probes that combine both BBB permeability and ER targeting capability. Therefore, there is an urgent need to develop effective ONOO⁻

*School of Chemistry & School of Life Science and Engineering, Key Laboratory of Advanced Technologies of Material Ministry of Education, Southwest Jiaotong University, Chengdu 610031, People's Republic of China.
E-mail: ywwang@swjtu.edu.cn, pengyu@swjtu.edu.cn*
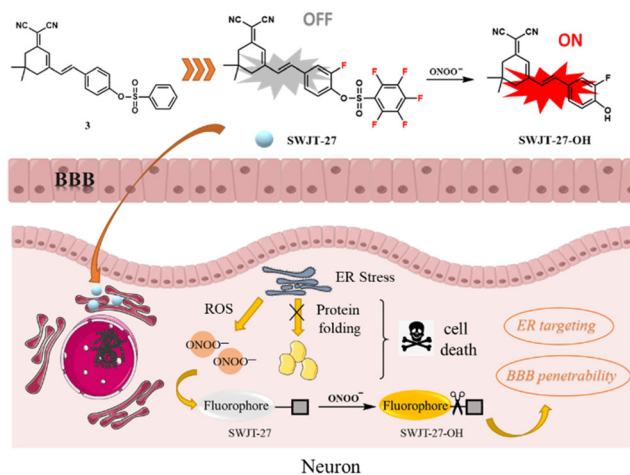†Represents equal contributions by both authors.

Fig. 1 Design and application of **SWJT-27** for sensing ONOO⁻.

fluorescent probes specifically for CIRI studies to break the biological limitation.

Herein, we synthesized a new ONOO⁻ fluorescent probe (**SWJT-27**) that could both cross the BBB and target the ER. As shown in Fig. 1, fluorination significantly enhanced the lipid solubility of the probe. **SWJT-27** has a substantial fluorescence enhancement ratio (425-fold), a low detection limit (9.492 nM), high sensitivity, and excellent selectivity for ONOO⁻ detection. In addition, the BBB penetration ability of the probe was verified using an *in vitro* BBB model. Finally, it was successfully applied to ONOO⁻ imaging in cells and living organisms of the ER.

Results and discussion

Synthesis of SWJT-27

The synthesis route and spectrum are shown in Scheme S1 and Fig. S1–S3. Compounds **2** and **SWJT-27-OH** were synthesized according to previous reports.[31,32]

Synthesis of compound 3. Compound **2** (200.0 mg, 0.69 mmol) was dissolved in DCM (5 mL), followed by the addition of benzenesulfonyl chloride (121.7 mg, 0.69 mmol). Then, 3 drops of triethylamine were added dropwise. The reaction mixture was stirred at room temperature for 15 minutes, and the crude product was purified by column chromatography (PE : EA = 10 : 1) on silica gel. To further purify the product, a mixed system of DCM and petroleum ether was used for recrystallization and filtered to obtain **3** as a yellow solid (234.1 mg, 79% yield). ¹H NMR (600 MHz, chloroform-*d*): δ = 7.86 (d, *J* = 7.8 Hz, 2H), 7.71 (t, *J* = 7.5 Hz, 1H), 7.56 (t, *J* = 7.7 Hz, 2H), 7.44 (d, *J* = 8.3 Hz, 2H), 7.03 (d, *J* = 8.3 Hz, 2H), 7.00 (d, *J* = 16.1 Hz, 1H), 6.92 (d, *J* = 16.1 Hz, 1H), 6.85 (s, 1H), 2.62 (s, 2H), 2.46 (s, 2H), 1.09 (s, 6H). ¹³C NMR (150 MHz, chloroform-*d*): δ = 169.13, 153.22, 150.12, 135.26, 135.12, 134.76, 134.46, 130.17, 129.27, 128.69, 128.48, 124.13, 123.02, 113.33, 112.58, 79.36, 42.98, 39.19, 32.04, 28.00.

Compound **SWJT-27** was obtained as a yellow solid (79% yield) using the same method for the synthesis of compound **3**. ¹H NMR (400 MHz, chloroform-*d*) δ = 7.47–7.39 (m, 1H), 7.37–7.27 (m, 2H), 6.96 (s, 2H), 6.90 (s, 1H), 2.64 (s, 2H), 2.47 (s, 1H), 1.11 (s, 6H). ¹³C NMR (100 MHz, chloroform-*d*) δ = 168.77, 155.38, 152.87, 152.24, 137.50, 137.43, 136.29, 136.16, 133.37, 131.93, 125.39, 125.05, 124.24, 124.20, 115.49, 115.30, 113.06, 112.32, 80.41, 42.94, 39.20, 32.04, 27.98. ESI-MS: *m/z* 537.0 [M − H]⁻.

Design and mechanism verification

Dicyanoisophorone was selected as the fluorophore due to its optimal properties, including a large Stokes shift, a near-infrared emission profile, easy modification, and excellent biocompatibility.[33–37] Benzenesulfonate ester is a fluorescence quenching group commonly used for specific recognition of nucleophilic substances. It has excellent specificity, remarkable stability, and effective fluorescence shielding properties.[38–40] These advantageous characteristics enable its successful application for ONOO⁻ visualization recognition in both cellular systems and live organisms. Therefore, as shown in Fig. 1, the fundamental architecture of the probe is formed by the combination of dicyanoisophorone and benzenesulfonate.

To enable ER-specific monitoring during CIRI, the probe requires two critical functions: BBB permeability and ER-targeting capability. Extensive studies have confirmed that elevated lipophilicity served as a key structural determinant for these two properties. On the one hand, high lipid-soluble small molecule compounds are more likely to cross the BBB by passive diffusion.[26] On the other hand, ER membranes favor the solubilization of lipid-soluble fluorescent probes.[41] The ER membrane is enriched in cholesterol, sphingolipids, and phospholipids. Small molecules with high lipid solubility are more easily dissolved in the lipid bilayer of the ER due to their low polarity and high hydrophobicity, thus passively accumulating in the ER membrane or lumen.[42,43] On this basis, the lipid–water partition coefficient ($c \log P$) for compound **3** was calculated to be only 0.76 using the octanol–water system. To enhance this performance, **SWJT-27** was obtained by introducing multiple fluorine atoms into the structure of compound **3**. Compared to other halogens, the fluorine atom has the smallest relative molecular weight, making it easier for the probe to cross the BBB.[25] The $c \log P$ of **SWJT-27** was 2.02, much higher than that of compound **3** (Fig. S4). The results suggested that **SWJT-27** had great potential for BBB penetration and ER targeting.
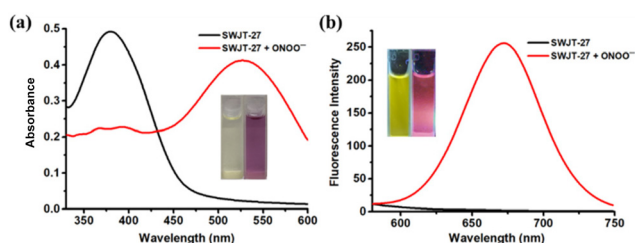
To elucidate the reaction mechanism between **SWJT-27** and ONOO⁻, mass spectrometry (MS) experiments were conducted. As demonstrated in Fig. S5 and S6, the MS profiles of **SWJT-27** treated with ONOO⁻ exhibited almost-identical data to **SWJT-27-OH**, which supported a mechanism wherein ONOO⁻ nucleophilically attacked the recognition group, inducing cleavage of the O–S bond and subsequent formation of **SWJT-27-OH**. To further investigate the relationship between the probe and the spectra, the generalized density function was

calculated using Gaussian 09. As shown in Fig. S7, compared with **SWJT-27**, the energy gap between HOMO and LUMO of **SWJT-27-OH** was smaller, suggesting that the absorption spectrum of **SWJT-27** underwent a red shift when reacting with ONOO⁻. The result was consistent with the UV–vis spectrum.
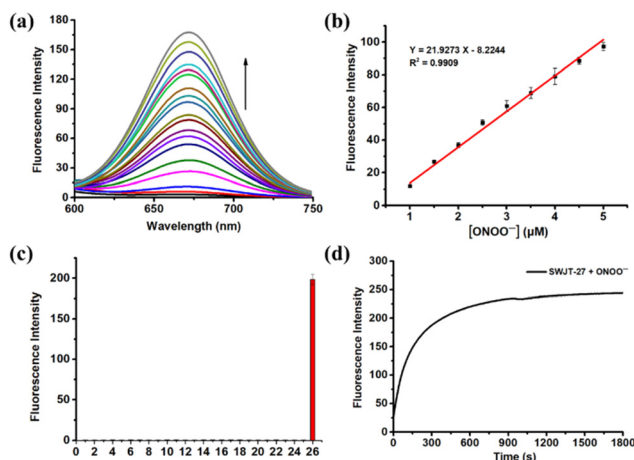
Spectral responses

The experimental conditions for **SWJT-27** were optimized through sequential screening assays. By initial solvent screening through fluorescence spectroscopy dimethyl sulfoxide (DMSO) was determined to be the optimal organic phase (Fig. S8). Subsequently the evaluation of aqueous buffers demonstrated that the fluorescence intensity was significantly enhanced in HEPES buffer compared to other buffers (Fig. S9). Phase ratio optimization revealed that a 1 : 1 (v/v) organic/aqueous mixture was the most effective solution (Fig. S10). pH-dependent fluorescence studies conducted in HEPES buffer at pH 3.0–10.0 showed that the fluorescence enhancement was greatest between pH 7.0 and 10.0 (Fig. S11). To maintain biological relevance, pH 7.4 was selected for all subsequent experiments to approximate intracellular conditions. Under these conditions, UV–Vis spectral analysis of **SWJT-27** (Fig. 2a) showed a red-shift of the absorption maximum from 380 nm to 530 nm, accompanied by a visible colorimetric change from yellow to purple. As shown in Fig. 2b, after adding ONOO⁻ to the solution containing **SWJT-27**, the fluorescence emission at 670 nm showed a remarkable 425-fold enhancement, and the quantum yield Φ increased from 0.03% to 2.45%. And the solution color changed from yellow to red. As presented in Fig. S12 and Table S1, probe **3** exhibited similar reaction patterns to **SWJT-27**. However, the fluorescence enhancement of **3** after reacting with ONOO⁻ was not significant. These results preliminarily verified the specific response of **SWJT-27** to ONOO⁻.

In Fig. 3a, the sensitivity of **SWJT-27** toward ONOO⁻ was quantitatively evaluated through fluorescence titration experiments. The gradual addition of ONOO⁻ to the solution containing **SWJT-27** induced a concentration-dependent enhancement of fluorescence emission at 670 nm. A linear calibration curve was established (Fig. 3b), yielding a detection limit of 12.205 nM (S/N = 3), indicating higher sensitivity for ONOO⁻

Fig. 3 (a) Fluorescence spectra of **SWJT-27** (10.0 μM, λ_{ex} = 540 nm) in the presence of various concentrations of ONOO⁻ (0.0–10.0 μM). (b) Fluorescence intensity as a function of [ONOO⁻]. (c) Responses of **SWJT-27** upon the addition of different substances (100.0 μM). From left to right: 1: blank, 2: Na⁺, 3: Mg²⁺, 4: K⁺, 5: Cu²⁺, 6: Cl⁻, 7: F⁻, 8: Br⁻, 9: I⁻, 10: Fe²⁺, 11: Fe³⁺, 12: NO₂⁻, 13: S²⁻, 14: SO₃²⁻, 15: HSO₃⁻, 16: CH₃COO⁻, 17: H₂O₂, 18: ·OH, 19: ¹O₂, 20: O₂·⁻, 21: ClO⁻, 22: Cys, 23: Hcy, 24: GSH, 25: Glu and 26: ONOO⁻. (d) Response time of **SWJT-27** to ONOO⁻.

detection.[44–46] Selectivity experiments revealed that when **SWJT-27** was added to various biologically relevant analytes, the fluorescence response was minimal (Fig. 3c). These results confirmed that **SWJT-27** had excellent molecular specificity. The response time of **SWJT-27** with ONOO⁻ was then tested. As shown in Fig. 3d, the maximum fluorescence was achieved within 15 minutes, which was much faster than that of **3** (Fig. S13). Pseudo-primary kinetic diagrams were plotted as presented in Fig. S14, and the rate constant was obtained (K_{obs} = 4.4 × 10⁻³ s⁻¹). Moreover, a 30-minute fluorescence test was performed on the solution of **SWJT-27** to examine its stability in Fig. S15. As shown in Fig. S16, **SWJT-27** exhibited a strong response to ONOO⁻ following 2 hours of co-incubation, while showing no reactivity toward other tested substances. These results demonstrated that **SWJT-27** had good sensitivity, selectivity and stability in ONOO⁻ recognition.

Imaging of ONOO⁻ in cells

Firstly, the biocompatibility of **SWJT-27** was assessed through cell viability assays. CCK-8 analysis in HeLa and HT22 cells showed that after culturing with different concentrations of **SWJT-27** for 24 h, the survival rate of cells was >90% (Fig. S17 and S18), confirming the minimal cytotoxicity under experimental conditions. To evaluate the ONOO⁻ detection capability of **SWJT-27**, fluorescence imaging was performed in both HeLa and HT22 cell models. As shown in Fig. 4a, **SWJT-27** showed almost no fluorescence in the control group. As the concentration of **SWJT-27** increased, the fluorescence intensity of HeLa cells induced by LPS gradually increased. After the addition of ROS inhibitors (NAC), the red fluorescence decreased significantly. Corresponding fluorescence intensity

Fig. 2 (a) UV–vis absorption and (b) emission spectra of **SWJT-27** (10.0 μM, λ_{ex} = 540 nm) in HEPES buffer (50% DMSO, pH = 7.4) solution in the absence and presence of ONOO⁻ (10.0 μM). Inset: photos of **SWJT-27** without (left) or with (right) ONOO⁻ under (a) visible light or (b) 365 nm UV light.

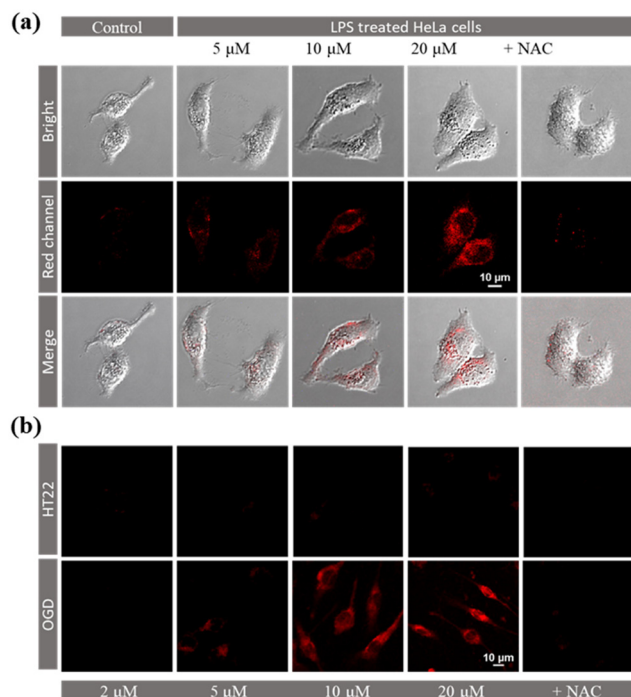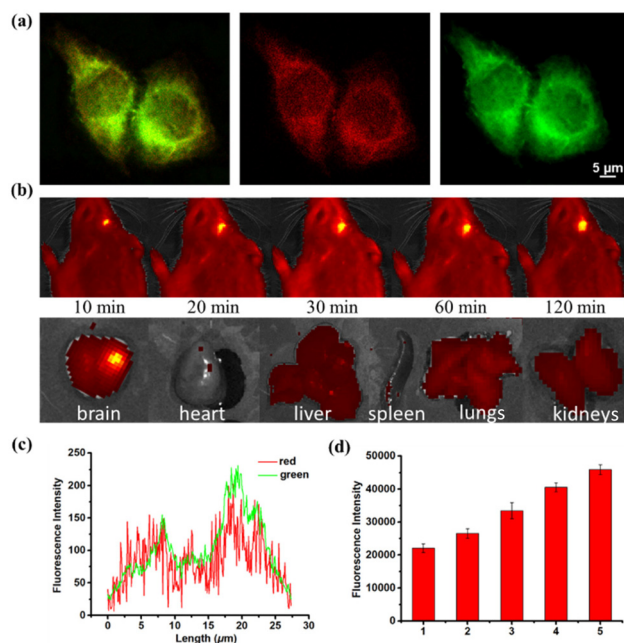**Fig. 4** (a) Fluorescence imaging of HeLa cells treated with varying concentrations of **SWJT-27**. (b) Fluorescence imaging of HT22 cells and OGD models treated with varying concentrations of **SWJT-27**.

Fig. 5 (a) ER co-localization experiments of **SWJT-27** (10.0 μM). **SWJT-27** along with a commercially available green ER fluorescent probe (10.0 μM) were co-incubated with HeLa cells for 30 min and then imaged. (b) Time-dependent imaging of **SWJT-27** (8 mg kg^{-1}) in the MACO model and the experimental group after undergoing dissection and then imaging. From left to right are: the brain, heart, liver, spleen, lungs, and kidneys. (c) Line graphs of the green and red channels. (d) Quantitative analysis of the fluorescence intensity using ImageJ software. The error bars represent the standard deviation ($\pm$S.D.), n = 3.

changes are shown in Fig. S19. To better simulate the CIRI conditions, parallel experiments were conducted using HT22 neural cells and oxygen-glucose deprivation (OGD) models. As shown in Fig. 4b and Fig. S20, HT22 neurons subjected to OGD exhibited strong dose-dependent fluorescence after **SWJT-27** treatment, while the signal in the normoxic control group was negligible. These results confirmed that **SWJT-27** had excellent ONOO$^-$ imaging capabilities in hypoxic and hypoglycemic cellular environments.

Based on the favorable lipophilicity of **SWJT-27**, ER co-localization experiments were performed. HeLa cells were co-stained with **SWJT-27** (red channel) and the commercial ER-tracker (green channel), followed by confocal microscopy imaging after 30 minutes of incubation. As shown in Fig. 5a, the red fluorescence of **SWJT-27** overlapped well with the green fluorescence of the commercial dye, and the Pearson coefficient was calculated to be 0.92. The corresponding line graphs are shown in Fig. 5C. These results confirmed the precise ER-targeting capability of **SWJT-27**. Finally, to verify whether **SWJT-27** could cross the BBB, an *in vitro* BBB model was constructed using immortalized mouse brain microvascular endothelial cells (b. End3). The probe was added to the upper chamber, and the fluorescence intensity of the lower chamber was measured using a multifunctional enzyme-linked immunosorbent assay (ELISA) after 4 hours. As shown in Fig. S21, the apparent permeability coefficient (Papp) of **SWJT-27** was calculated to be 1.4623×10^{-5} cm s^{-1}, which indicated that **SWJT-27** was sufficient to penetrate the BBB.

Imaging of ONOO$^-$ *in vivo*

The excellent cell imaging performance of **SWJT-27** had prompted its application for *in vivo* monitoring of ER stress during CIRI. Firstly, a middle cerebral artery occlusion (MCAO) model was established in a rat. After 1 hour of reperfusion, ONOO$^-$ imaging in its brain was performed *via* intravenous injection of **SWJT-27**. As shown in Fig. 5B, fluorescence imaging revealed pronounced signal accumulation in the ischemic hemisphere, indicating that **SWJT-27** had crossed the BBB and acted on the site of CIRI lesions. Time-dependent experiments showed that the fluorescence intensity gradually increased within 2 hours after injection, which was correlated with ongoing ER stress and ONOO$^-$ generation during reperfusion. Corresponding fluorescence intensity changes are shown in Fig. 5d. After dissection, imaging showed that the fluorescence site was consistent with the brain site. These results suggested that **SWJT-27** is a suitable tool for real-time visualization of ER stress and ONOO$^-$ production *in vivo*.

Conclusions

In conclusion, the traditional ONOO$^-$ recognition probe was transformed into a highly lipid-soluble fluorescent probe through rational structural modifications. This modification

endowed the probe (**SWJT-27**) with both BBB penetration capability and ER-targeting specificity. In addition, **SWJT-27** exhibited significant advantages including near-infrared emission, substantial fluorescence enhancement, and excellent selectivity. Moreover, **SWJT-27** was successfully employed for ONOO⁻ identification and detection in the ER of rat MCAO models.

Experimental

All general methods are listed in the SI.

Conflicts of interest

There are no conflicts of interest to declare.

Data availability

All related data generated and/or analyzed during the current study are available from the corresponding author upon reasonable request.

Supplementary information is available: spectral data, copies of $^1H/^{13}C$ NMR, HRMS and other materials. See DOI: **https://doi.org/10.1039/d5ob01119a**.

Acknowledgements

References

1 S. K. Feske, Ischemic stroke, *Am. J. Med.*, 2021, **134**, 1457–1464.

2 C. Johnson, M. Nguyen, G. Roth, *et al.*, *Lancet Neurol.*, 2019, **18**, 439–458.

3 Z. Chen, Y. Li and X. Liu, *Biomed. Pharmacother.*, 2023, **169**, 115839.

4 Q. Zhang, M. Jia, Y. Wang, Q. Wang and J. Wu, *Neurochem. Res.*, 2022, **47**, 3525–3542.

5 S. Elmore, *Toxicol. Pathol.*, 2007, **35**, 495–516.

6 X. Luo, S. Cheng, W. Zhang, K. Dou, R. Wang and F. Yu, *ACS Sens.*, 2024, **9**, 810–819.

7 Y. Han, M. Yuan, Y. Guo, X. Shen, Z. Gao and X. Bi, *Front. Cell. Neurosci.*, 2021, **15**, 704334.

8 G. Ferrer-Sueta, N. Campolo, M. Trujillo, S. Bartesaghi, S. Carballal, N. Romero, B. Alvarez and R. Radi, *Chem. Rev.*, 2018, **118**, 1338–1408.

9 A. Korkmaz, H. Yaren, T. Topal and S. Oter, *Arch. Toxicol.*, 2006, **80**, 662–670.

10 D. Rachmilewitz, J. S. Stamler, F. Karmeli, M. E. Mullins, D. D. Singel, J. Loscalzo, R. J. Xavier and D. K. Podolsky, *Gastroenterology*, 1993, **105**, 1681–1688.

11 H. Y. Chung, H. J. Kim, K. W. Kim, J. S. Choi and B. P. Yu, *Microsc. Res. Tech.*, 2002, **59**, 264–272.

12 G. Ferrer-Sueta and R. Radi, *ACS Chem. Biol.*, 2009, **4**, 161–177.

13 C. Szabó, H. Ischiropoulos and R. Radi, *Nat. Rev. Drug Discovery*, 2007, **6**, 662–680.

14 L. Wang, M. S. Frei, A. Salim and K. Johnsson, *J. Am. Chem. Soc.*, 2019, **141**, 2770–2781.

15 A. R. Knight, E. L. Taylor, R. Lukaszewski, K. T. Jensen, H. E. Jones, J. E. Carre, M. N. Isupov, J. A. Littlechild, S. J. Bailey, E. Brewer, T. J. McDonald, A. R. Pitt, C. M. Spickett and P. G. Winyard, *Free Radical Biol. Med.*, 2018, **120**, 246–254.

16 W. Imaram, C. Gersch, K. M. Kim, R. J. Johnson, G. N. Henderson and A. Angerhofer, *Free Radical Biol. Med.*, 2010, **49**, 275–281.

17 P. Wang, L. Yu, J. Gong, J. Xiong, S. Zi, H. Xie, F. Zhang, Z. Mao, Z. Liu and J. S. Kim, *Angew. Chem., Int. Ed.*, 2022, **61**, e202206894.

18 Y. Y. Li, J. L. Hu, J. R. Wu, Y. R. Wang, A. H. Zhang, Y. W. Tan, Y. J. Shang, T. Liang, M. Li, Y. L. Meng and Y. F. Kang, *Biosens. Bioelectron.*, 2024, **254**, 116233.

19 D. Wei, Y. Dai, X. Yan, D. Lan, J. Liao, Z. Qin and N. Fu, *ACS Sens.*, 2025, **10**, 2542–2553.

20 L. Xing, B. Wang, J. Li, X. Guo, X. Lu, X. Chen, H. Sun, Z. Sun, X. Luo, S. Qi, X. Qian and Y. Yang, *J. Am. Chem. Soc.*, 2022, **144**, 2114–2119.

21 Q. Chen, L. Shen, J. L. Cui, X. H. Liu, H. Y. Zou, X. Q. Cao, S. L. Shen and X. F. Zhang, *Sens. Actuators, B*, 2025, **422**, 136686.

22 Y. Zhu, C. Liu, X. Rong, M. Zheng, H. Wen, K. Wang, W. Sheng and B. Zhu, *Sens. Actuators, B*, 2025, **439**, 137774.

23 B. Wang, Y. Kong, X. Tian and M. Xu, *J. Hazard. Mater.*, 2024, **469**, 134094.

24 W. Zhang, J. Liu, P. Li, X. Wang, S. Bi, J. Zhang, W. Zhang, H. Wang and B. Tang, *Biomaterials*, 2019, **225**, 119499.

25 D. Tang, M. Liu, Z. Wen, N. Xu, L. Zhao, J. Wu, F. Yu and H. Liu, *Sens. Actuators, B*, 2025, **423**, 136826.

26 R. L. Teleanu, M. D. Preda, A. G. Niculescu, O. Vladâcenco, C. I. Radu, A. M. Grumezescu and D. M. Teleanu, *Pharmaceutics*, 2022, **14**, 987.

27 S. Ding, A. I. Khan, X. Cai, Y. Song, Z. Lyu, D. Du, P. Dutta and Y. Lin, *Mater. Today*, 2020, **37**, 112–125.

28 G. C. Terstappen, A. H. Meyer, R. D. Bell and W. Zhang, *Nat. Rev. Drug Discovery*, 2021, **20**, 362–383.

29 P. C. Trippier, *Curr. Med. Chem.*, 2016, **23**, 1392–1407.

30 R. Pandit, L. Chen and J. Götz, *Adv. Drug Delivery Rev.*, 2020, **165–166**, 1–14.

31 L. Kong, Q. Bai, C. Li, Q. Wang, Y. Wang, X. Shao, Y. Wei, J. Sun, Z. Yu, J. Yin, B. Shi, H. Fang, X. Chen and Q. Chen, *Nat. Commun.*, 2024, **15**, 9413.

32 Y. Geng, H. Zhang, G. Zhang, J. Zhou, M. Zhu, L. Ma, X. Wang, T. D. James and Z. Wang, *Anal. Chem.*, 2023, **95**, 11943–11952.

33 D. Shen, W. Jin, Y. Bai, Y. Huang, H. Lyu, L. Zeng, M. Wang, Y. Tang, W. Wan, X. Dong, Z. Gao, H. Piao, X. Liu and Y. Liu, *Angew. Chem., Int. Ed.*, 2021, **60**, 16067–16076.

34 Y. Yang, M. Ma, L. Shen, J. An, E. Kim, H. Liu, M. Jin, S. Wang, J. Zhang, J. S. Kim and C. Yin, *Angew. Chem., Int. Ed.*, 2023, **62**, e202310408.

35 H. Yan, Y. Wang, F. Huo and C. Yin, *J. Am. Chem. Soc.*, 2023, **145**, 3229–3237.

36 Y. Zhao, K. Wei, F. Kong, X. Gao, K. Xu and B. Tang, *Anal. Chem.*, 2018, **91**, 1368–1374.

37 Y. Shi, F. Huo and C. Yin, *Sens. Actuators, B*, 2020, **325**, 128793.

38 D. Yuan, K. Pan, S. Xu and L. Wang, *Anal. Chem.*, 2022, **94**, 12391–12397.

39 B. Li, H. Mei, M. Wang, X. Gu, J. Hao, X. Xie and K. Xu, *Dyes Pigm.*, 2021, **189**, 109231.

40 X. Xia, Y. Qian and B. Shen, *J. Mater. Chem. B*, 2018, **6**, 3023–3029.

41 W. Shu, S. Zang, C. Wang, M. Gao, J. Jing and X. Zhang, *Anal. Chem.*, 2020, **92**, 9982–9988.

42 C. Gao, Y. Tian, R. Zhang, J. Jing and X. Zhang, *Anal. Chem.*, 2017, **89**, 12945–12950.

43 H. Zhou, J. Tang, L. Sun, J. Zhang, B. Chen, J. Kan, W. Zhang, J. Zhang and J. Zhou, *Sens. Actuators, B*, 2019, **278**, 64–72.

44 W. Yang, R. Liu, X. Yin, Y. Jin, L. Wang, M. Dong, K. Wu, Z. Yan, G. Fan, Z. Tang, Y. Li and H. Jiang, *Sens. Actuators, B*, 2023, **393**, 134180.

45 W. Feng and G. Feng, *Dyes Pigm.*, 2019, **164**, 174–181.

46 J. Shang, Y. Yang, Y. Sun, W. Gao, K. Ma, C. Wang, X. Yu, L. Li, J. Zheng, N. Zhao, X. Shu and Y. Zhang, *Redox Biol.*, 2025, **80**, 103494.